J. Fluid Mech. (2005), *vol.* 534, *pp.* 327–350.
doi:10.1017/S0022112005004659 Printed in the United Kingdom

Relaminarization phenomena and external-disturbance effects in spherical Couette flow

By KOICHI NAKABAYASHI[1], WEIMING SHA[2] AND YOICHI TSUCHIDA[3]

[1]Department of Mechanical Systems Engineering, Aichi University of Technology, Manori 50-2, Nishihazama-cho, Gamagori City, 443-0047, Japan

[2]Geophysical Institute, Graduate School of Science, Tohoku University, Aoba-ku, Sendai, 980-8578, Japan

[3]Engineering Physics, Electronics and Mechanics, Graduate School of Engineering, Nagoya Institute of Technology, Gokiso-cho, Showa-ku, Nagoya, 466-8555, Japan

(Received 9 May 2003 and in revised form 31 January 2005)

The relaminarization phenomenon in the laminar–turbulent transition process of spherical Couette flow with the inner sphere rotating and the outer sphere fixed has been experimentally investigated for $0.06 \leqslant \beta \leqslant 0.206$, where β is the ratio of the clearance to the inner-sphere radius. The relaminarization occurs for $0.13 < \beta < 0.17$, and is observed as a reverse Hopf bifurcation from the limit cycle to the fixed point. The kinetic energy in the high-frequency region of the fluctuating azimuthal velocity component continues to increase with Reynolds number Re in the case without relaminarization, but in the case with relaminarization it first increases and then decreases with increasing Re and finally vanishes with the onset of the relaminarization. For $\beta = 0.14$ with relaminarization, a small artificial disturbance introduced externally into the spherical Couette flow has no influence on the lowest critical Reynolds number of the first instability that can be defined universally and uniquely. On the other hand, the external disturbance decreases the onset Reynolds numbers of both the second instability (occurrence of spiral Taylor–Görtler (TG) vortices) and the relaminarization, although it has no influence on the fundamental frequencies of velocity fluctuation caused by spiral TG vortices and travelling waves on TG vortices.

1. Introduction

The equatorial regions in the spherical Couette flow (SCF) between two concentric spheres with the inner sphere rotating and the outer sphere at rest show dynamical behaviour similar to that in the circular Couette flow (CCF) with the inner cylinder rotating, while the polar regions in SCF show dynamical behaviour similar to that in the flow around a rotating disk in a container. Therefore, the transition phenomena of SCF are strongly dependent on gap widths and more complex than those of CCF. Most of the previous studies on SCF were restricted to cases of small and medium gap widths in which the first instability occurs as Taylor vortices at the equator (e.g. Munson & Menguturk 1975; Wimmer 1976; Nakabayashi 1978; Yavorskaya *et al.* 1980; Krause 1980; Nakabayashi 1983; Belyaev *et al.* 1984; Bühler & Zierep 1984, 1987; Marcus & Tuckerman 1987*a*, *b*; Wimmer 1988; Nakabayashi & Tsuchida 1988*a*, *b*; Bühler 1990; Dumas & Leonard 1994; Nakabayashi *et al.* 1994;

Nakabayashi & Tsuchida 1995; Zikanov 1996; Nakabayashi, Morinishi & Kobayashi 1997; Nakabayashi & Sha 2000; Sha & Nakabayashi 2001; Nakabayashi, Tsuchida & Zheng 2002*a*; Nakabayashi, Zheng & Tsuchida 2002*b*, *c*). Recently, some experimental and theoretical studies were also conducted on wide gap widths in which the first instability occurs in the form of non-axisymmetric spiral waves called spiral vortices (for example, Dumas & Leonard 1994; Egbers & Rath 1995; Araki, Mizushima & Yanase 1997; Wulf, Egbers & Rath 1999).

Thus the flow structures caused by the first instability differ with gap size. The vortex structure occurring during the transition process also differs greatly below and above $\beta \approx 0.3$. Here, β is defined as $(R_2 - R_1)/R_1$, where R_1 and R_2 are the radii of the inner and outer spheres, respectively. Toroidal Taylor–Görtler (TG) vortices occur for $\beta < 0.3$, but not for $\beta > 0.3$. For $\beta < 0.3$ treated in the present study, the transition processes involving the evolution of the vortical structures with increasing Reynolds number Re obviously differ between $\beta < 0.1$ and $\beta > 0.2$ (Nakabayashi *et al.* 2002*a*, *c*).

In the laminar–turbulent transition for $\beta < 0.2$, no velocity fluctuation occurs until spiral TG vortices (note: different from the spiral vortices occurring in the wide gap) occur in supercritical flow with increasing Re. As Re is increased further after the occurrence of the velocity fluctuation, the velocity fluctuation increases with Re, and finally the flow becomes turbulent. Thus, periodic, quasi-periodic, chaotic and fully developed turbulent velocity fluctuations occur successively with increasing Re for $\beta < 0.2$ (Nakabayashi *et al.* 2002*a*). For $\beta = 0.14$, however, the velocity fluctuation occurring with spiral TG vortices at low Reynolds numbers disappears completely with increasing Re (the relaminarization phenomenon), although, with a further increase of Re, the velocity fluctuation reappears and evolves to a fully developed turbulent flow (Nakabayashi & Tsuchida 1988*a*). The transition scenario leading to the relaminarization phenomenon for $\beta = 0.14$ was revealed by so-called chaos dynamics, i.e. by investigating the attractor in a Poincaré section of the phase space of velocity fluctuation and the evolution of the correlation dimension with increasing Re (Nakabayashi *et al.* 1994). The chaos-dynamics method has been used as a powerful method to analyse the transition process of dissipation systems. For example, Brandstater & Swinney (1987) and Belyaev & Yavorskaya (1991) applied the method to analysing the correlation dimension, the maximum Lyapunov exponent, etc. to clarify the transition process of flow in Couette systems, and characterized the behaviour of the chaotic flow. Subsequently, Nakabayashi *et al.* (1997) studied the details of the transition scenario and the one-dimensional return map for $\beta = 0.14$. However, it has not yet been clarified in what ranges of β and Re the relaminarization phenomenon (i.e. the disappearance of velocity fluctuation with increasing Re) occurs, and what is the mechanism for the relaminarization.

On the other hand, the Taylor instability was clarified to be of the pitchfork-bifurcation type for $\beta < 0.3$ by linear stability theory (Mamun & Tuckerman 1995). However, the values of the critical Reynolds number differ among the results of experiments and numerical simulations. The first critical Reynolds number seems to change due to an external small disturbance introduced artificially. Is there a universal value for the first critical Reynolds number? Moreover, it is interesting to explore how the second and third instabilities are changed by this external disturbance. So, we consider the receptivity of the transition process by introducing a sufficiently small artificial disturbance into SCF from outside.

In the present study, in order to investigate the reason for the occurrence of relaminarization in the case of a quasi-static increase of the rotation rate of the inner

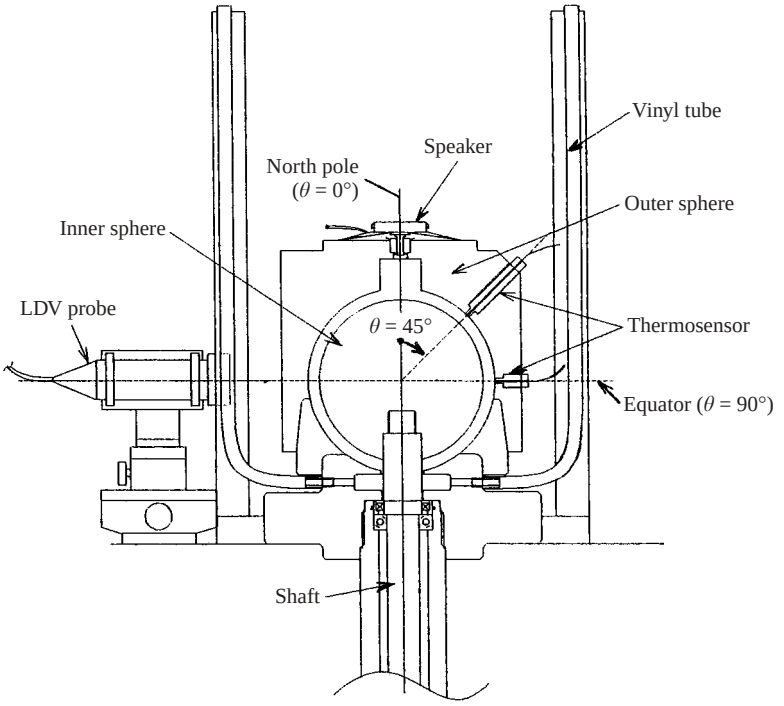

FIGURE 1. Experimental apparatus. The speaker installed above the north pole (colatitude $\theta = 0°$) is used to introduce the external disturbance into the flow.

sphere, we use an experimental method to consider in what ranges of β and Re the relaminarization phenomenon occurs, and investigate what differences exist between two kinds of transition processes: with and without the relaminarization. We also compare the bifurcation diagram obtained from the probability density distribution of the velocity fluctuation between the two kinds of transition processes. The velocity fluctuation disappearance is revealed to be a reverse-bifurcation phenomenon. We obtain the lowest critical Reynolds number of the first instability that can be determined universally by introducing a sufficiently small artificial disturbance into SCF from outside.

2. Experimental apparatus and method

In the present experiment, velocity measurements were performed by a laser Doppler velocimeter for five clearance ratios, $\beta = 0.06, 0.10, 0.14, 0.158$, and 0.206. The experimental apparatus shown in figure 1 is substantially the same as that used in earlier studies (Nakabayashi 1983; Nakabayashi & Tsuchida 1988*a*). The inner and outer spheres are made of aluminium alloy and transparent acrylic resin, respectively. The Reynolds number is defined as $Re = \hat{U}_0 R_1/\nu = 2\pi \hat{f}_0 R_1^2/\nu$, where $\hat{f}_0$ is the rotation frequency of the inner sphere, $\hat{U}_0$ $(= 2\pi \hat{f}_0 R_1)$ is the peripheral speed at the equator of the inner sphere, and ν is the kinematic viscosity of the working fluid. The temperature of the working fluid was measured by two thermosensors located at the meridian angles (colatitudes) $\theta = 45°$ and $90°$ (equator), and the temperature fluctuation was controlled within $\pm 0.1\,°\mathrm{C}$ so as to have no perceptible influence on the transition process. The radius R_1 of the inner sphere and the critical Reynolds number Re_C of the Taylor instability are tabulated in table 1 for each clearance ratio β, where the

β	R_1 (mm)	Re_C
0.06	82.55 ± 0.04	2760
0.10	79.74 ± 0.03	1440
0.14	76.88 ± 0.03	900
0.158	75.71 ± 0.03	760
0.206	72.67 ± 0.04	554

TABLE 1. Radius R_1 of the inner sphere and the critical Reynolds number Re_C for each clearance ratio β. The radius R_2 of the outer sphere is fixed to be 87.65 ± 0.03 mm.

radius of the outer sphere is fixed at $R_2 = 87.65 \pm 0.03$ mm for all β. For each β, the accuracies of the whip of the rotating inner sphere and the concentricity of the inner and outer spheres were within ± 0.02 mm. Hence, the whip and concentricity were too small to affect the laminar–turbulent transition (Nakabayashi 1983; Nakabayashi & Tsuchida 1988*a*). Water and a glycerol–water solution of 50% mass-concentration were used as the working fluids.

In order to investigate the flow state in the quasi-static transition from rest, the acceleration of Reynolds number $\mathrm{d}R^*/\mathrm{d}\hat{t}$ did not exceed $0.0006\,\mathrm{s}^{-1}$, where R^* is a reduced Reynolds number defined as Re/Re_C. The values of Re_C in table 1 were obtained under the this acceleration condition by flow-visualization measurements. The Re_C values for $\beta = 0.06$ and 0.206 agree with those in Nakabayashi (1983). In the present study, another reduced Reynolds number R_1^* defined as Re/Re_{C1} is also used for $\beta = 0.14$, where Re_{C1} (= 860) is the lowest critical Reynolds number defined in § 4.1.

In the present study, the frequency, time, and velocity scales are expressed in units of the inner-sphere rotation frequency $\hat{f}_0$, the inner-sphere rotation period $1/\hat{f}_0$, and the peripheral speed $\hat{U}_0$ at the equator of the inner sphere, respectively. Also, variables with hats have dimensions, and dimensionless variables are expressed without hats. For example, $\hat{f}$ and f $(= \hat{f}/\hat{f}_0)$ are dimensional and non-dimensional frequencies, respectively, of a fluctuating velocity component.

Velocity measurements were made for fluctuating azimuthal and meridian velocity components, $\hat{\tilde{V}}_\phi$ and $\hat{\tilde{V}}_\theta$, respectively, in the centre of the gap ($\eta = 0.5$) at the equator ($\theta = 90^\circ$), except in special cases defined explicitly. η, defined as $(r - R_1)/(R_2 - R_1)$, is the dimensionless wall distance from the inner-sphere wall, where r is a radial coordinate.

We obtained the correlation dimension d of the fluctuating azimuthal velocity $\hat{\tilde{V}}_\phi$ as follows (Nakabayashi *et al.* 1997), where the correlation dimension gives a lower-limit value of freedom induced in the dynamic system (Berge, Pomeau & Vidal 1984). First the trajectory (attractor) in an m-dimensional phase space was calculated from the dimensionless time series records $X(t)$ (made up of $\tilde{V}_\phi$) by the delay-time method: $X(t) = [X(t), X(t+\tau), \ldots, X(t+(m-1)\tau)]$, where τ is the delay time, and m is the embedded dimension. The probability $C(r)$ that this data point on the attractor is included inside a sphere with centre $x(i)$ and radius r on the attractor was calculated using the following equation:

$$C(r) = (1/M)\sum_{i=1}^{i=M} C_i(r), \text{ where } C_i(r) = (1/N)\sum_{j=1}^{j=N} H(r - |x(i) - x(j)|). \qquad (1)$$

N is the total number of data points; M is the number of data points selected arbitrarily on the attractor; and H is the Heaviside function. Finally, the correlation

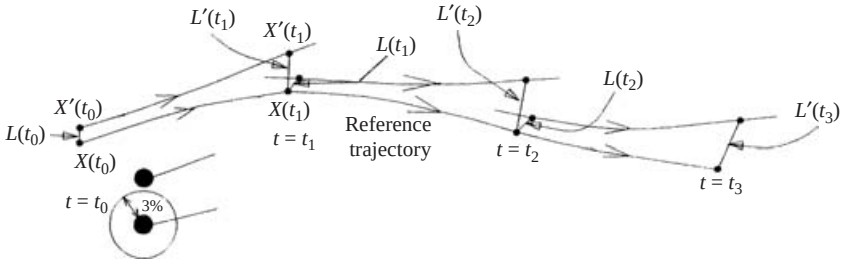

FIGURE 2. Schematic representation of the evolution and replacement procedure to obtain the maximum Lyapunov exponent λ.

dimension d was obtained by

$$d = \lim_{r \to 0} \log C(r) / \log r, \tag{2}$$

where d converges to a constant value with increasing m. In the present study, $m = 2$–17; $N = 4000$–20000; $M = 1000$; and the optimal delay time τ was determined as the time at which the next joint information function $I(\tau)$ first has a minimum value with an increase in τ, following Fraser & Swinney (1986):

$$I(\tau) = \int\int P(y, z) \log_2 [P(y, z)/\{P(y)P(z)\}] \, \mathrm{d}y \, \mathrm{d}z, \text{ with } y = X(t), \mathrm{z} = X(t + \tau), \tag{3}$$

where $P(y)$ and $P(z)$ are probability density functions, and $P(y, z)$ is their combined probability function.

The maximum Lyapunov exponent λ was obtained using the algorithm of Wolf *et al.* (1985), following Nakabayashi *et al.* (1997) (also see figure 2). Although n Lyapunov exponents exist in the n-dimensional phase space, we focused only on the maximum Lyapunov exponent in the present study, where the maximum Lyapunov exponent quantifies the sensitivity to initial conditions and its sensitivity is characteristic of the chaotic behaviour. First, we reconstruct the trajectory in an m-dimensional phase space, as described previously: $X(t) = [X(t), X(t + \tau), \ldots, X(t + (m - 1)\tau)]$, utilizing values up to eight for the embedded dimension m. Secondly, at time $t = t_0$, we select the initial record $X(t_0)$ on the reference trajectory, and record $X'(t_0)$ that is more than 3 % of the maximum amplitude of $\tilde{V}_\phi$ and is the nearest to $X(t_0)$, obtaining the distance $L(t_0)$ between $X(t_0)$ and $X'(t_0)$. Thirdly, at time t_1 after one period of the attractor from time t_0, for example, $t_1 = t_0 + 1/f_S$ in the case where the attractor is mainly due to spiral TG vortices whose fundamental frequency is f_S, we find the distance $L'(t_1)$ between $X(t_1)$ and $X'(t_1)$, and obtain the ratio $L'(t_1)/L(t_0)$. Next, at time t_1, we again select a new record $X'(t_1)$ neighbouring $X(t_1)$ on the reference trajectory, obtaining the distance $L(t_1)$ between $X(t_1)$ and $X'(t_1)$. Then, by calculating the next time segment ($t_2 = t_1 + 1/f_S$), we obtain $L'(t_2)/L(t_1)$. By repeating this procedure over the whole reference trajectory until time t_M, the maximum Lyapunov exponent λ is derived from the following equation:

$$\lambda = \{1/(t_M - t_0)\} \sum_{k=1}^{k=M} L'(t_k)/L(t_{k-1}). \tag{4}$$

From the value of λ, we see the type of attractor: limit cycle or T^2 torus for $\lambda = 0$, and strange (or chaotic) attractor for $\lambda > 0$.

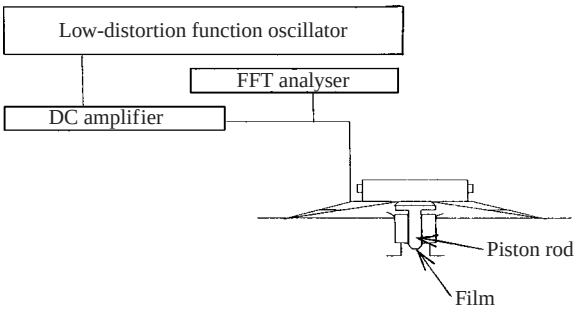

FIGURE 3. Speaker system to introduce the external disturbance into the flow.

We introduced a sufficiently small artificial external disturbance into the flow by oscillating the piston rod connected to the speaker installed above the north pole (see figure 1). Details of the speaker system are given in figure 3. The speaker frequency was set as $\hat{f}_I = 1$–7 Hz, high enough for fundamental frequencies, approximately 0.1–2 Hz, of spiral TG vortices and travelling waves on TG vortices that are related to the relaminarization (Nakabayashi & Tsuchida 1988*a*). The amplitude of the piston rod was kept at a small constant value so that the amplitude of the fluctuating meridian velocity component of the external disturbance caused by the rod is less than approximately 1/50 times that caused by spiral TG vortices, although it depends slightly on the value of $\hat{f}_I$. The external disturbance was verified to be almost uniformly propagated over the whole spherical gap by monitoring the fluctuating meridian velocity component at $R^* = 0$.

3. Differences between transition processes with and without relaminarization

3.1. *Region of occurrence of relaminarization*

The evolution of the azimuthal velocity fluctuation $\tilde{V}_\phi$ with increasing R^* is shown for $\beta = 0.10$ in figure 4(*a*) as an example of a case in which relaminarization does not occur and for $\beta = 0.158$ in figure 4(*b*) as a case in which it occurs. In figure 4(*a*), the velocity fluctuation begins as a periodic one at $R^* = 1.06$, and the amplitude and complexity of the fluctuation gradually increase with an increase in R^*. Therefore, relaminarization does not occur. In figure 4(*b*), on the other hand, the velocity fluctuation changes from a periodic one to a complicated one, with increasing R^*, but then the complexity decreases and finally a periodic fluctuation ($R^* = 4.65$) reappears. If R^* is further increased, the velocity fluctuation completely disappears, i.e. relaminarization occurs. In spherical Couette flow, this interesting relaminarization phenomenon was first observed for $\beta = 0.14$ (Nakabayashi & Tsuchida 1988), while for circular Couette flow, so far as we know, there has been no report in the literature about it. In the case of the Lorenz system however, Argyris, Faust & Haase (1994) observed a periodic window within a chaotic region as in the case of the logistic map. According to Argyris *et al.*, the periodic window emerges as a result of an inverse cascade of periodic halvings, and the periodic motion loses its stability at higher Rayleigh numbers.

Figure 5 shows isograms of the correlation dimension $d = 1$, 2 and 3 in the $(Re - \beta)$-plane. Figure 5 also shows data for the occurrence and/or disappearance of spiral TG vortices, travelling waves on TG vortices, and shear waves obtained by flow-visualization measurements. The transition Reynolds numbers of the generation and

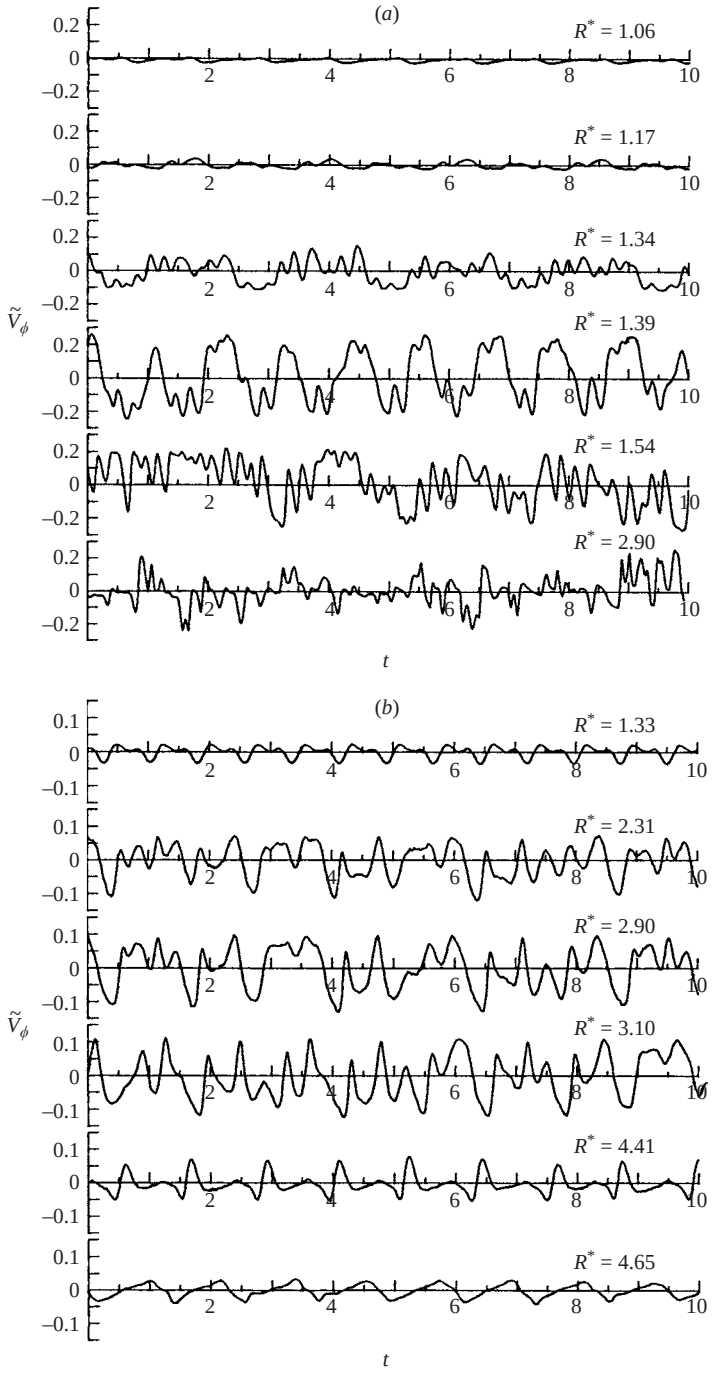

FIGURE 4. Examples of the evolution of $\tilde{V}_\phi$ with increasing R^*, where t is dimensionless time. (*a*) $\beta = 0.10$ without relaminarization. (*b*) $\beta = 0.158$ with relaminarization.

disappearance of spiral TG vortices are consistent with the isogram of $d = 1$, and those of travelling waves are consistent with $d = 2$. From this figure, it is proven that the range of β in which relaminarization occurs is approximately 0.13–0.17.

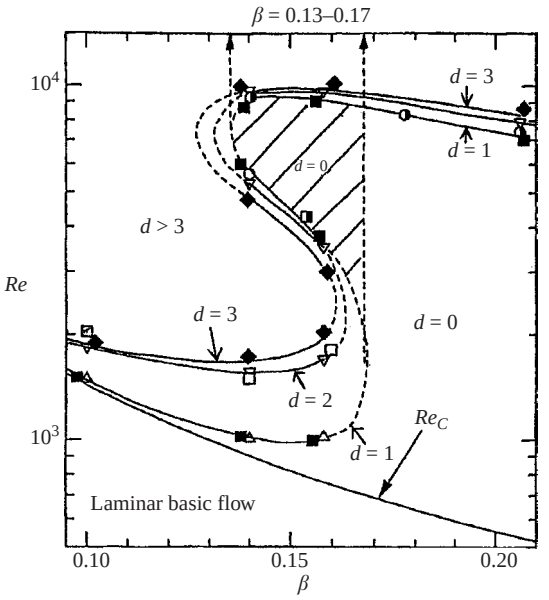

FIGURE 5. Isograms of the correlation dimension d, and data for the occurrence and disappearance of various disturbances in the $(Re-\beta)$-plane. The region of velocity-fluctuation disappearance is hatched. ■, $d=1$; --∇--, $d=2$; --◆--, $d=3$; ◑, occurrence of shear waves ($\beta=0.1779$, Bühler & Zierep 1987); ○, disappearance of disturbance; ◨, disappearance of travelling waves ($\beta=0.154$, Bühler 1990); □, occurrence of travelling waves; Δ, occurrence of spiral TG vortices.

3.2. *Evolution of correlation dimension and maximum Lyapunov exponent*

Figure 6 shows the Reynolds-number dependence of the correlation dimension d and the maximum Lyapunov exponent λ for four clearance ratios, $\beta=0.06$, 0.14, 0.158 and 0.206. At $R^*=1$ for all β, steady toroidal TG vortices are generated. At the first arrow on the left side of each figure, spiral TG vortices occur for $\beta=0.06$, 0.14 and 0.158, and interior waves occur inside toroidal TG vortices for $\beta=0.206$.

In the case of $\beta=0.06$ in figure 6(a), for about $R^*=1.1$–1.2, $\lambda>0$ and the value of d is 1.5, but the dispersion of the λ value is large. These results are due to electrical noise because, in this R^* region, the signal level of the velocity fluctuation is very small compared with the noise level. For $R^*=1.22$–1.30, however, the dispersion of λ vanishes, and we can obtain the result that $\lambda=0$ and $d=1$. Hence, the measurement had been accurately carried out, and it was proven that the trajectory formed a limit cycle in this R^* region. For $R^*>1.3$, on the other hand, $\lambda>0$ and d rapidly increases to more than 3. This indicates the generation of a strange attractor.

In the case of $\beta=0.14$ in figure 6(b), λ is zero within the region $1.0<R^*<1.2$ and the attractor is a fixed point in the phase space which corresponds to the toroidal TG vortex. λ is almost zero in the R^* ranges ($1.20<R^*<1.74$ and $1.74<R^*<1.95$) showing $d=1$ and $d=2$, and their attractors are a limit cycle and T^2 torus, respectively. Afterwards, d rapidly increases to about 5 because λ has a large positive value. Therefore, the attractor is characteristic of a strange attracter corresponding to low-dimensional chaos. For $R^*=5.5$–5.8, d decreases to about 2.5, but λ remains positive. For $R^*=5.8$–5.9 just before relaminarization occurs, d decreases to almost 1 at the same time as λ decreases to almost zero. A limit cycle is then formed in the phase

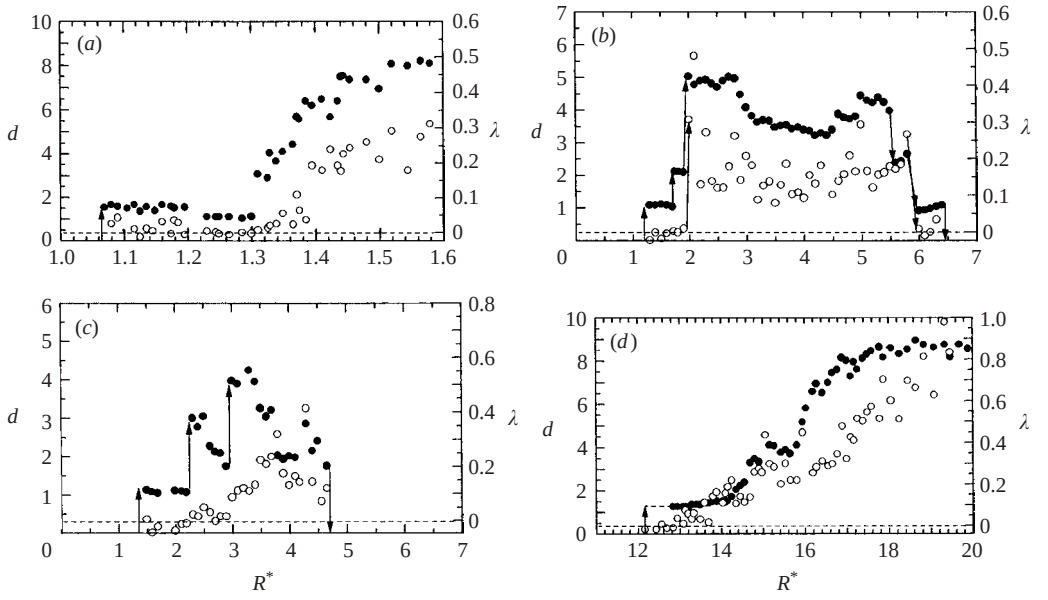

FIGURE 6. Evolution of correlation dimension d (●), and maximum Lyapunov exponent λ (○) with increasing R^*. (*a*) $\beta = 0.06$. (*b*) $\beta = 0.14$ (relaminarization). (*c*) $\beta = 0.158$ (relaminarization). (*d*) $\beta = 0.206$.

space. As R^* increases further ($R^* = 6.8$), d becomes zero and the successive attractor is a fixed point, i.e. relaminarization occurs.

Similarly to the case of $\beta = 0.14$, for the case of $\beta = 0.158$ as seen in figure 6(*c*) a limit cycle is first formed for $d = 1$ with $\lambda \doteqdot 0$. With increasing R^*, d increases to about 3 with $\lambda > 0$, but d decreases to 2 with $\lambda \doteqdot 0$, so that a T^2 torus is formed. With a further increase in R^*, d decreases to 1.8 with $\lambda > 0$. Finally, d becomes zero and a fixed point is formed as relaminarization occurs.

In the case of $\beta = 0.206$ in figure 6(*d*), d tends to increase from near $R^* = 12.5$, but it is not as clear. For about $R^* = 13$, d is a little larger than 1 with $\lambda \neq 0$, so that the limit cycle cannot be formed. Then, d and λ continues to increase with R^*.

3.3. *Evolution of the kinetic energy of fluctuation*

The evolution of the power spectra $E(f)$ of the azimuthal velocity fluctuation with increasing R^* is shown for $\beta = 0.06$ in figure 7(*a*) and for $\beta = 0.158$ in figure 7(*b*) as representative cases where relaminarization does not occur and occurs, respectively. In the case of $\beta = 0.06$ without relaminarization, a peak value appears at the frequency f_{S1} or f_{S2} due to spiral TG vortices with the number of vortex pairs S_P of 2 or 1, respectively, at low Reynolds numbers ($R^* < 1.31$), and harmonics of f_{S1} or f_{S2} begin to show more definite peak values with increasing R^*. Here, f_{S1} and f_{S2} were confirmed to be fundamental frequencies of the spiral TG vortices with $S_P = 2$ and 1, respectively, by flow-visualization measurements and simultaneous measurements of laser light scattering (for more details see Nakabayashi *et al.* 2002*a*). At high Reynolds numbers ($R^* \geqslant 1.31$), however, peak values appear at f_B due to the fluctuation of the outflow boundary of TG vortices and at f_{W1}, f_{W2} or f_{W3} due to travelling waves with wavenumber m of 8, 10 or 11, respectively. Simultaneously, harmonics and integer-linear combinations of f_B and f_W appear. f_B was confirmed to agree with the

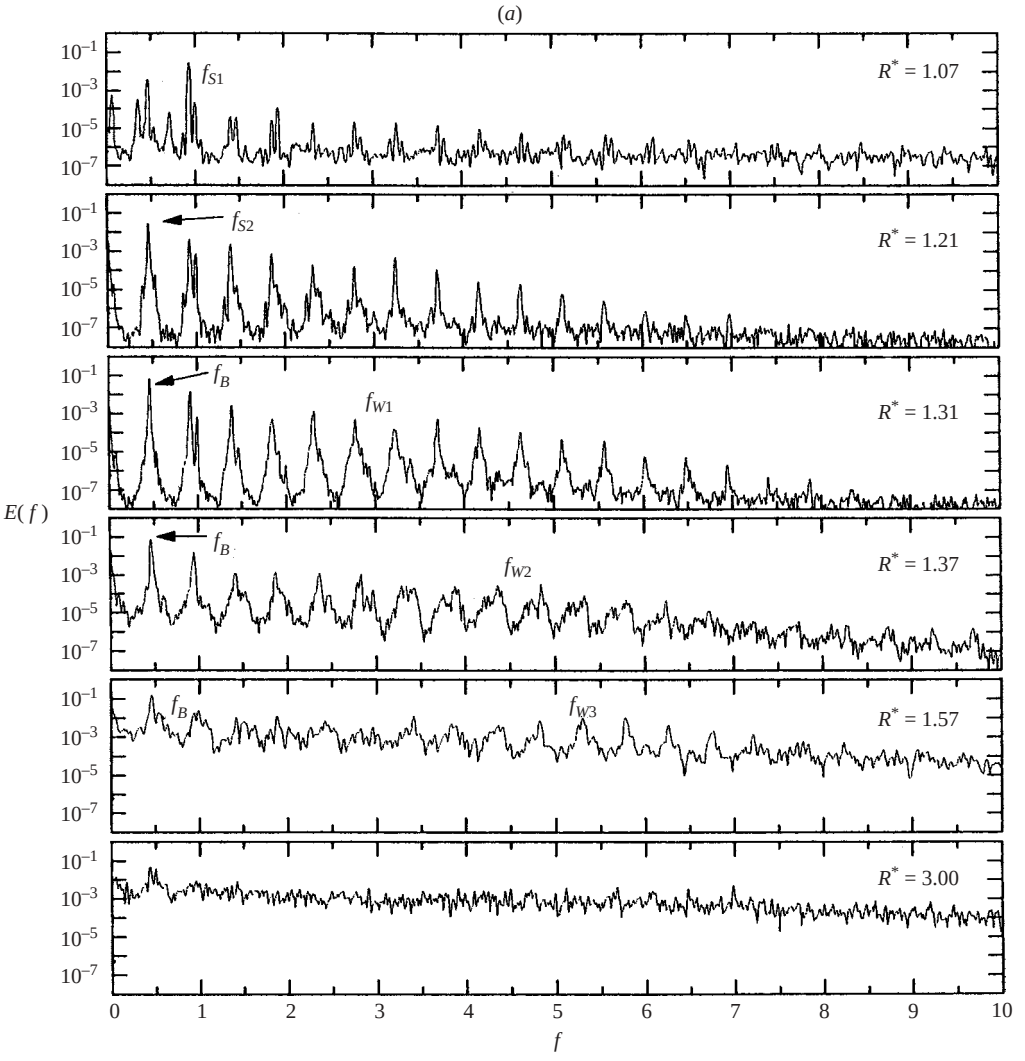

FIGURE 7(*a*). For caption see facing page.

rotation frequency of spiral TG vortices with the same time-dependent vortex-pair number at $R^* = 1.31$ or 1.37 (Nakabayashi *et al.* 2002*a*). In the case of $\beta = 0.158$ with relaminarization, on the other hand, a peak value appears at f_{S1} due to spiral TG vortices with $S_P = 3$ at low Reynolds numbers ($R^* = 1.33$), and peak values appear at f_{S2} due to spiral TG vortices with $S_P = 2$ and at f_W due to six travelling waves ($m = 6$) on TG vortices at high Reynolds numbers ($R^* = 2.31$–4.65).

As seen in figure 7, the peak value due to spiral TG vortices (f_S) (or fluctuation of the vortex outflow boundary f_B) appears at about $f = 1$, and the dominant harmonics spread to the high-frequency side with an increase in R^*, while that due to travelling waves on TG vortices (f_W) appears at $f > 2$. Hence, let $f = 2$ between two fundamental frequencies f_S and f_W of spiral TG vortices and travelling waves, respectively, be a threshold value f_{th} between low- and high-frequency regions, and let us compare the energy E_{low} and E_{high} in the low- and high-frequency regions,

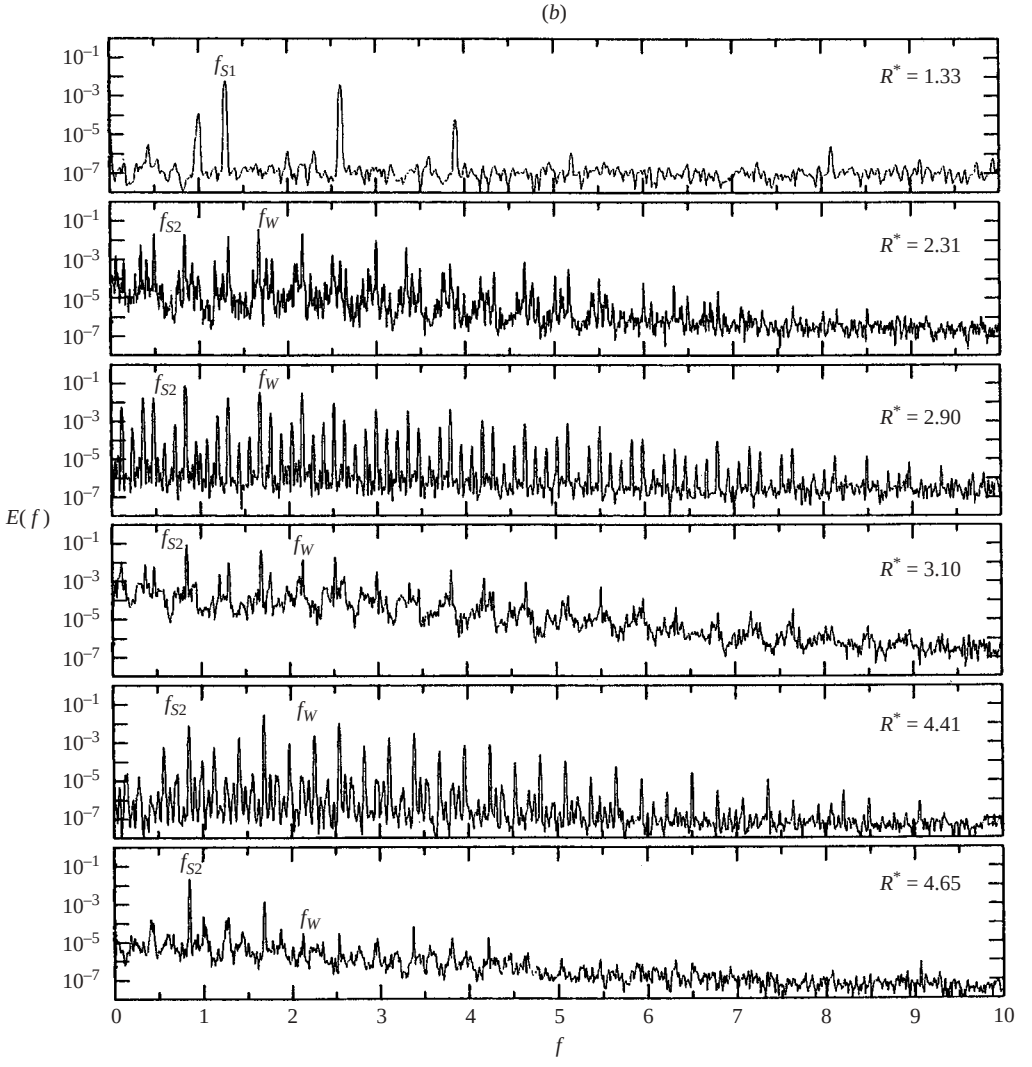

FIGURE 7. Evolution of power spectra $E(f)$ with increasing R^*. (*a*) $\beta = 0.06$ without relaminarization. (*b*) $\beta = 0.158$ with relaminarization.

defined as

$$E_{\text{low}} = \int_{0.1}^{2} E(f)\,\mathrm{d}f, \tag{5}$$

$$E_{\text{high}} = \int_{2}^{\infty} E(f)\,\mathrm{d}f. \tag{6}$$

E_{low} in (5) is the kinetic energy of disturbances in the low-frequency region $f < f_{th}$ including that of spiral TG vortices, while E_{high} in (6) is the kinetic energy of disturbances in the high-frequency region $f > f_{th}$ including that of travelling waves.

E_{low} and E_{high} are shown for $\beta = 0.06$, 0.14, and 0.158 in figures 8(*a*), 8(*b*) and 8(*c*), respectively. In the case of $\beta = 0.06$ without relaminarization, E_{high} is almost zero at low Reynolds numbers, and begins to gradually increase when the kinetic energy

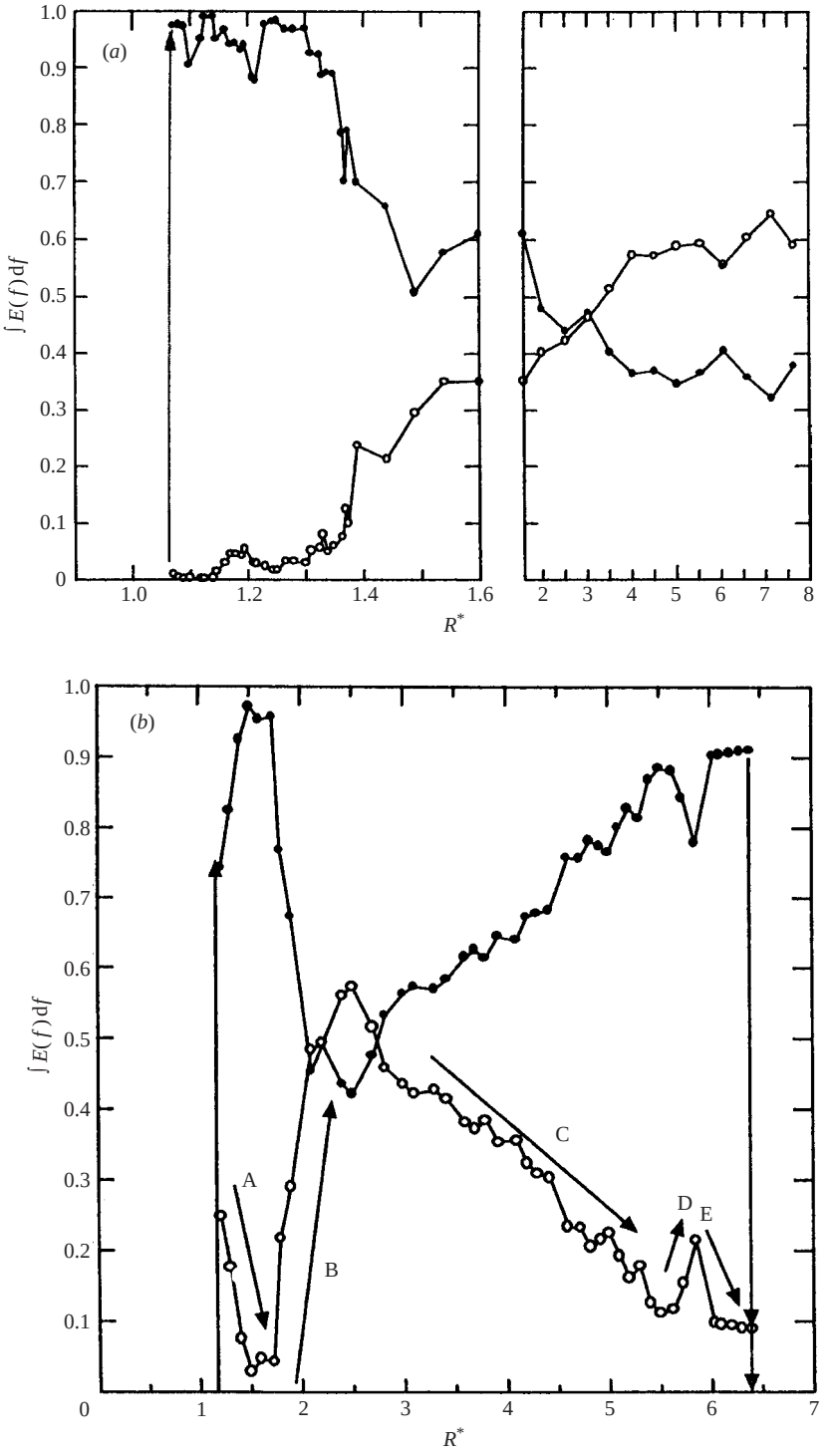

FIGURE 8(*a*, *b*). For caption see facing page.

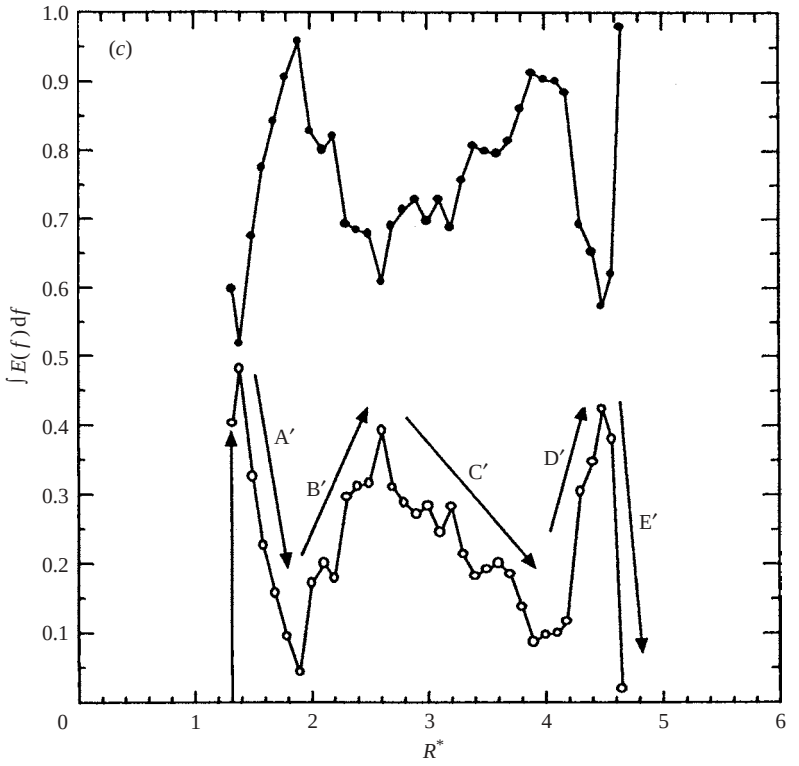

FIGURE 8. R^*-dependence of the kinetic energies E_{low} and E_{high} of disturbances in the lower and higher frequency regions, respectively. ●, E_{low}; ○, E_{high}. (*a*) $\beta = 0.06$. (*b*) $\beta = 0.14$ (relaminarization). A, C and E, decrease of E_{high}; B and D, increase of E_{high}. (*c*) $\beta = 0.158$ (relaminarization). A′, C′ and E′, decrease of E_{high}; B′ and D′, increase of E_{high}.

due to travelling waves on TG vortices is added, while E_{low} is large at low Reynolds number, and decreases with increasing R^*. When R^* exceeds about 3, E_{high} becomes greater than E_{low}. In the case of $\beta = 0.14$ with relaminarization, on the other hand, E_{low} occupies most of the disturbance energy at low Reynolds numbers, while E_{high} begins to increase with R^* because of the occurrence of travelling waves, to become the same as E_{low} at about $R^* = 2$. However, E_{high} decreases from $R^* = 2.5$, and then becomes very small at $R^* = 5.5$–6.4 just before relaminarization occurs. A, C, and E in figure 8(*b*) show the decrease in energy, while B and D show the increase. In the case of $\beta = 0.158$ with relaminarization, E_{low} and E_{high} show similar changes to those for $\beta = 0.14$ described above, although the decrease (A′, C′, E′) and increase (B′, D′) of energy are different in magnitude from those ((A, C, E) and (B, D)) for $\beta = 0.14$.

As described above, the energy of disturbances in the high-frequency region continues to increase in the chaotic regime in the case where relaminarization does not occur (figure 8*a*), while the energy decreases to almost zero in the chaotic regime in the case where it occurs (figure 8*b*, *c*). The relaminarization mechanism is thought to be that travelling waves on TG vortices weaken in spite of increasing Reynolds number and the flow returns to a steady toroidal-TG-vortex flow through the sudden disappearance of spiral TG vortices at a particular Reynolds number. However, the dynamics of this relaminarization phenomenon remains unclear, and requires more study.

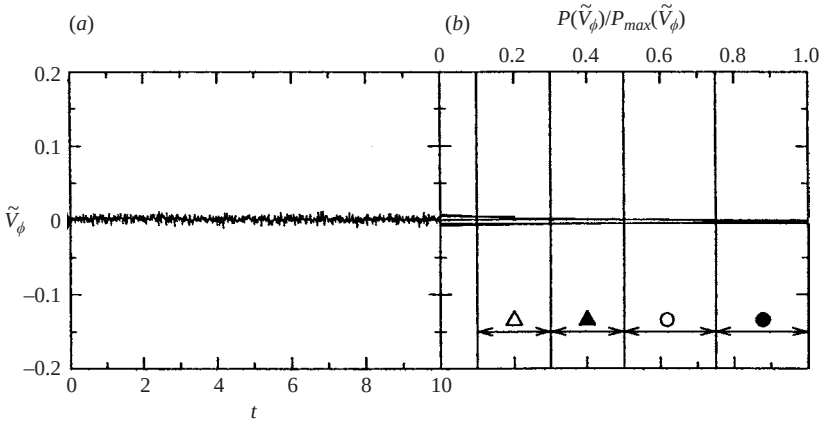

FIGURE 9. (*a*) Time-series records of $\tilde{V}_\phi$ and (*b*) the probability density distribution $P(\tilde{V}_\phi)$ used to make the bifurcation diagram at $R_1^* = 1.15$ for $\beta = 0.14$.

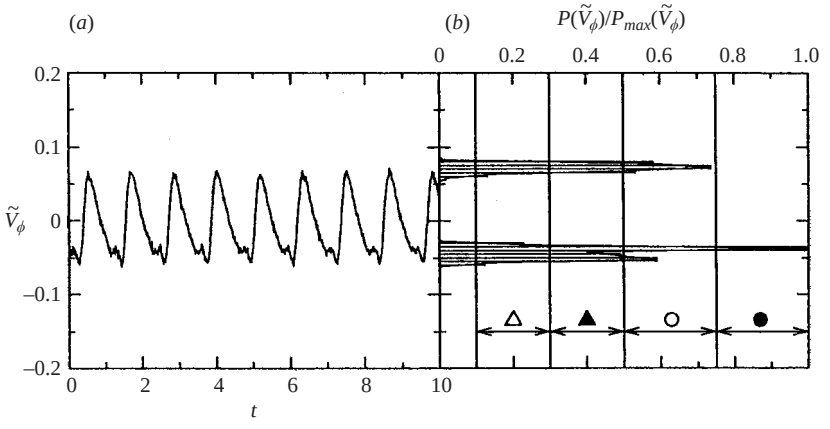

FIGURE 10. As in figure 9 but at $R_1^* = 1.39$.

3.4. *Bifurcation diagram*

3.4.1. *Case in which relaminarization occurs*

Now, we consider the bifurcation on the onset and disappearance of disturbances. Experimental research on the bifurcation was reported for $\beta = 0.33$ and 0.5 by Wulf *et al.* (1999). In the present study, bifurcation diagrams were constructed to examine the bifurcation for $\beta = 0.14$, 0.158 and 0.10, following Wulf *et al.*

In the case of $\beta = 0.14$ where relaminarization occurs, the first instability arises at $R_1^* = Re/Re_{C1} = 1.0$, so that steady toroidal TG vortices are formed near the equator. Next, spiral TG vortices are generated by the second instability at $R_1^* \approx 1.2$. The bifurcation for this second instability is a Hopf bifurcation (e.g. Berge *et al.* 1984), because a limit cycle is formed (Nakabayashi *et al.* 1994). At the onset of this second instability, the time series records of the azimuthal velocity fluctuation, $\tilde{V}_\phi(t)$, and the probability density distribution $P(\tilde{V}_\phi)$ change from those shown in figure 9 to figure 10. The third instability arises at $R_1^* \approx 1.8$ because the generation of travelling waves is confirmed from the velocity power spectra. At this third instability, $\tilde{V}_\phi(t)$ and $P(\tilde{V}_\phi)$

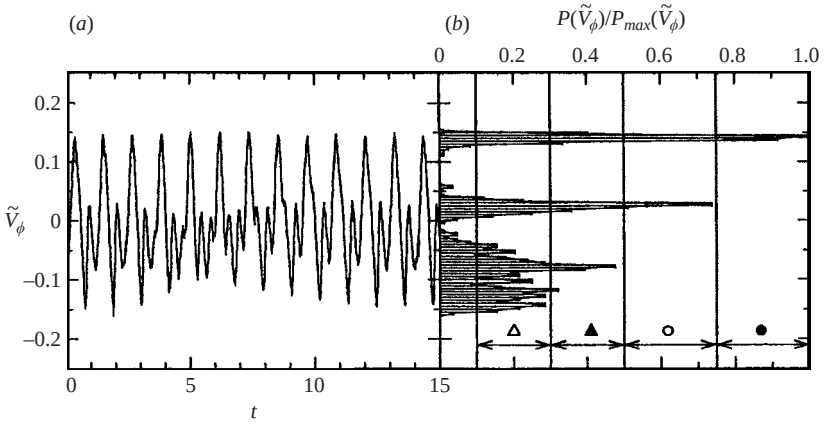

FIGURE 11. As in figure 9 but at $R_1^* = 1.87$.

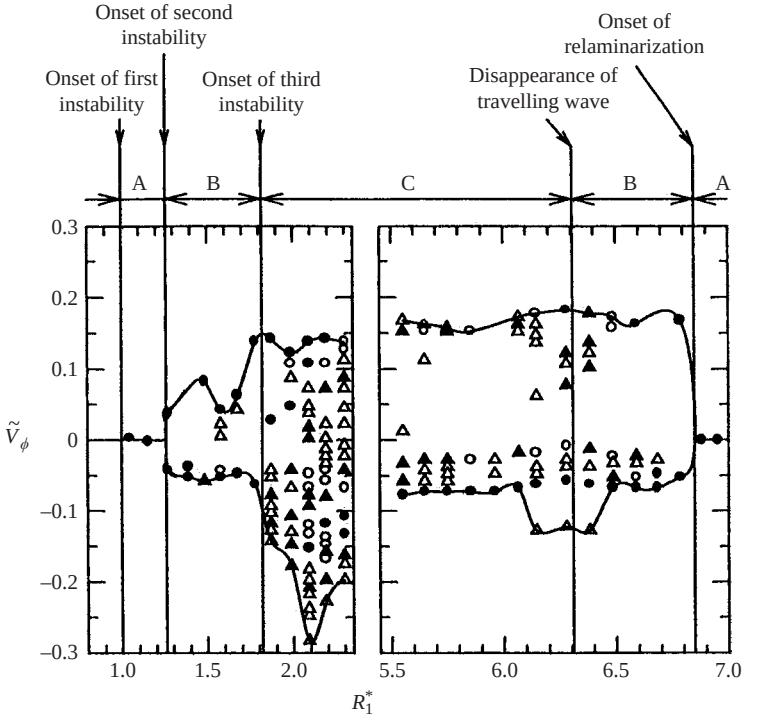

FIGURE 12. Bifurcation diagram in the case of $\beta = 0.14$ (relaminarization case). A, steady toroidal TG vortices; B, spiral TG vortices; C, spiral TG vortices and travelling waves on TG vortices. Δ, ▲, ○ and ● show ranges of the probability density scaled by its maximum value, $P(\tilde{V}_\phi)/P_{max}(\tilde{V}_\phi)$, at each Reynolds number, as shown in figures 9–11: Δ, $P(\tilde{V}_\phi)/P_{max}(\tilde{V}_\phi) =$ 0.1–0.3; ▲, 0.3–0.5; ○, 0.5–0.75; ●, 0.75–1.0.

change from figures 10 to 11, namely the probability density distribution changes in form from 2 to many peaks.

Figure 12 shows the bifurcation diagram for $\beta = 0.14$ obtained from $P(\tilde{V}_\phi)$ described above. Symbols Δ, ▲, ○ and ● in the figure present ranges of $P(\tilde{V}_\phi)$ shown in figures 9–11. In figure 12, we can confirm the reverse bifurcation from the transition from State B

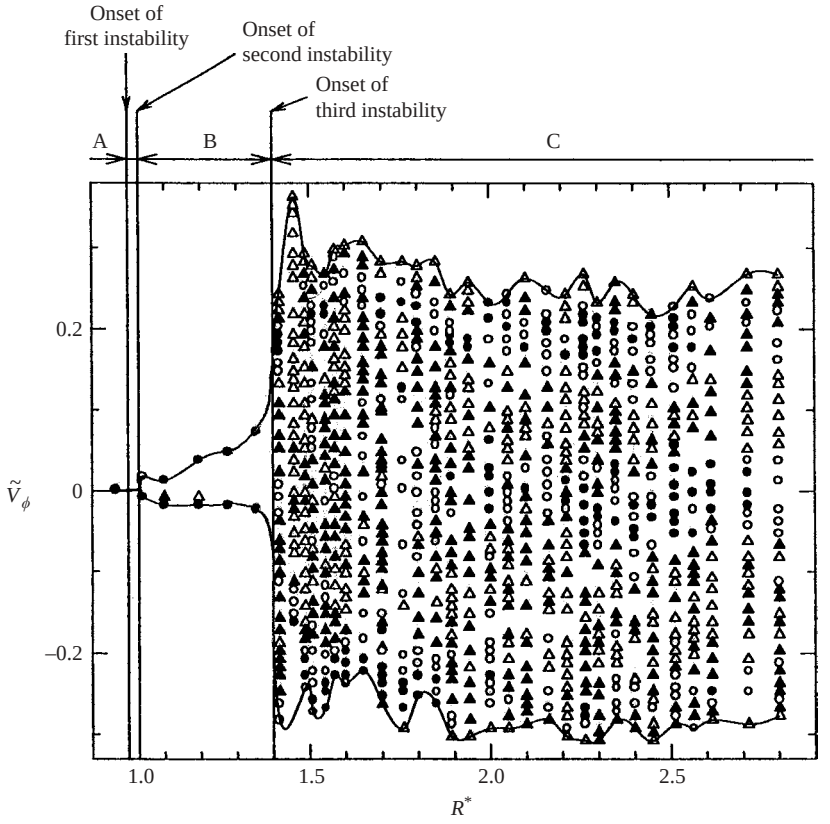

FIGURE 13. As in figure 12 but for $\beta = 0.10$ (no relaminarization case).

(time-dependent toroidal and spiral TG vortex flow) to State A (time-independent toroidal TG vortex flow) at $R_1^* \approx 6.8$ at which relaminarization arises. Thus, a limit cycle is formed before the onset of relaminarization and a fixed point is formed afterward (Nakabayashi *et al.* 1994). So, it is a reverse Hopf bifurcation because the attractor of the transition changes from the limit cycle to the fixed point. This kind of reverse Hopf bifurcation has been found in various fields, e.g. biology and optics (Longtin & Hinzer 1996; Larger *et al.* 2001) while it has never been reported for circular and spherical Couette flows. Although this reverse Hopf bifurcation has been observed for the first time, to our knowledge, in spherical Couette flow, the detailed explanation of the reverse Hopf bifurcation for this relaminarization phenomenon is beyond the scope of this work.

Also, for $\beta = 0.158$ a reverse Hopf bifurcation similar to that for $\beta = 0.14$ is perceived at $R^* \approx 4.85$.

3.4.2. *Case in which relaminarization does not occur*

Figure 13 shows the bifurcation diagram for $\beta = 0.10$ without relaminarization. Since the variations of $\tilde{V}_\phi(t)$ and $P(\tilde{V}_\phi)$ with the onsets of the second instability (Hopf bifurcation) and the third instability for $\beta = 0.10$ are similar to those for $\beta = 0.14$ in figures 9–11, the bifurcation diagram for $R^* = 1.0$–1.5 in figure 13 is similar to that for $R^* = 1.0$–2.0 in figure 12. However, since no relaminarization occurs for $\beta = 0.10$, no reverse bifurcation (transition from State B to State A) occurs in figure 13. This point is different from the cases of $\beta = 0.14$ with the relaminarization described above.

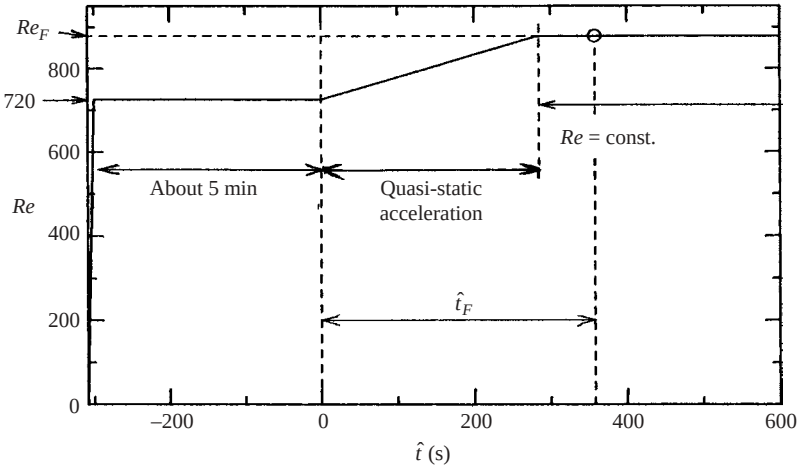

FIGURE 14. The condition for the time ($\hat{t}$) history of Re adopted to examine the lowest critical Reynolds number Re_{C1} for $\beta = 0.14$. Re_F and $\hat{t}_F$ are the primary onset Reynolds number and primary onset time, respectively.

4. External-disturbance effects on the transition process

4.1. *External-disturbance effect on the first instability* (*Taylor instability*)

The first instability at which toroidal TG vortices occur for $\beta < 0.3$ was revealed to be of supercritical-pitchfork type by linear stability theory (Mamun & Tuckerman 1995). However, there is a problem in that the critical Reynolds number of the first instability is different among numerical simulations and experiments, as mentioned previously. For $\beta = 0.14$, for example, the critical Reynolds number was theoretically determined to be 941 by numerical simulations (Sha & Nakabayashi 2001), while it was experimentally shown to be 923 by torque measurements (Nakabayashi 1978), and 880 (Nakabayashi & Tsuchida 1988*a*) and 900 (the present study) by flow-visualization measurements.

In order to consider the reason for the differences in the critical Reynolds number of the first instability, the following experiment was conducted for $\beta = 0.14$. Figure 14 shows the time history of Re taken from the experiment. First, Re is rapidly increased from zero to 720, and then is kept constant at 720 for about five minutes. Then, Re is increased to Re_F with a constant-acceleration condition $\mathrm{d}Re/\mathrm{d}\hat{t} \leqslant 0.54\,\mathrm{s}^{-1}$ that is thought to provide quasi-static acceleration, and then is kept constant at Re_F. During the experiment, the working fluid temperature is carefully kept constant. The critical Reynolds number of the first instability, $Re_C = 900$, for $\beta = 0.14$ in table 1 was determined as the Reynolds number at which toroidal TG vortices are formed when Re continues to increase with the above-mentioned acceleration, not as shown in figure 14. However, when Re is increased to Re_F as shown in figure 14, toroidal TG vortices can be formed gradually at time $\hat{t} = \hat{t}_F$ for $Re = Re_F$ even in the case with $Re < 900$. Such a vortex formation can also be seen in numerical simulations (Sha & Nakabayashi 2001). Therefore, Re_F and $\hat{t}_F$ are termed the primary onset Reynolds number and primary onset time, respectively.

The relationship between Re_F and $\hat{t}_F$ for various values of Re_F is shown by ○ for $\mathrm{d}Re/\mathrm{d}\hat{t} = 0.54\,\mathrm{s}^{-1}$, Δ for $0.45\,\mathrm{s}^{-1}$, □ for $0.36\,\mathrm{s}^{-1}$, and ◇ for $0.18\,\mathrm{s}^{-1}$ in figure 15 where each broken line indicates a curve connected with data under an assumption that Re_F approaches a constant value as $\hat{t}_F \to \infty$. Solid lines with double arrows show

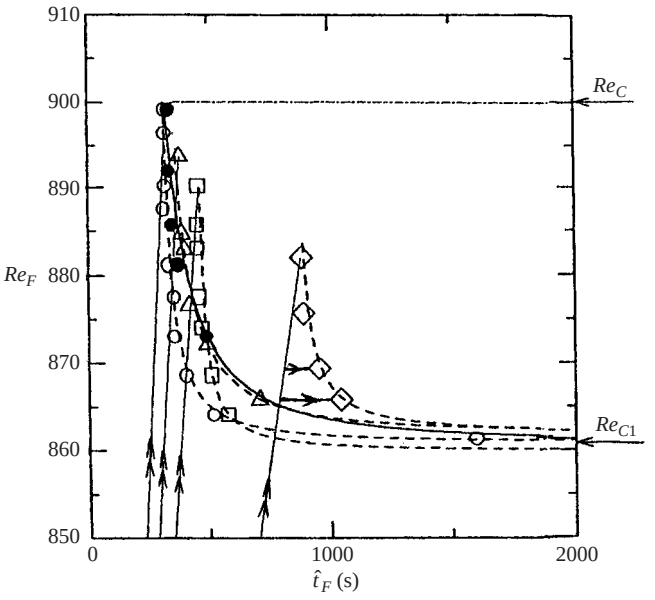

FIGURE 15. Relationship between the primary onset Reynolds number Re_F and the primary onset time $\hat{t}_F$ for various Re_F values for four quasi-static acceleration conditions $dRe/d\hat{t} = 0.54$ (indicated by ○), 0.45 (Δ), 0.36 (□), and 0.18 (◇) s^{-1} in the absence of the external disturbance, and for a quasi-static acceleration condition $dRe/d\hat{t} = 0.54\,s^{-1}$ (●) in the presence of the external disturbance with $\hat{f}_I = 5.0$ Hz. Broken lines guide the results of ($\hat{t}_F$, Re_F). Solid lines with double arrows show the relationship between Re (regarding Re_F as Re) and $\hat{t}_F$ during the four quasi-static accelerations. Thick solid lines each with a single arrow (shown only for $dRe/d\hat{t} = 0.18\,s^{-1}$ (◇)) show the relationship between Re_F and $\hat{t}_F$ at $Re = Re_F$. Re_C and Re_{C1} are the critical Reynolds number and the lowest one, respectively, of the first instability.

the relationship between Re (regarding the ordinate Re_F as Re) and $\hat{t}_F$ during the four quasi-static accelerations; and thick solid lines, each with a single arrow (shown only for $dRe/d\hat{t} = 0.18\,s^{-1}$), show the relationship between Re_F and $\hat{t}_F$ at $Re = Re_F$. Although the value of $Re_C = 900$ in table 1 is obtainable under the quasi-static acceleration condition of $dRe/d\hat{t} = 0.54\,s^{-1}$ with $Re_F = 900$, all the broken lines are thought to converge to the same value (about 860) of Re_F for $\hat{t}_F \to \infty$. Hence, this value of 860 is defined as the lowest critical Reynolds number of the first instability, Re_{C1}, which is obtainable under the condition that the first instability is allowed to take a long time to be established. This uniquely determined Re_{C1} is thought to give a universal critical Reynolds number. This lowest critical Reynolds number $Re_{C1} = 860$ is 7 % smaller than the conventional critical Reynolds number 923 obtained by torque measurements (Nakabayashi 1978), and is 9 % smaller than the 941 obtained by numerical simulations (Sha & Nakabayashi 2001), giving the lowest value of the critical Reynolds number.

Next, we investigate whether the influence of the external disturbance described previously affects the critical Reynolds number of the first instability, Re_C, and the lowest one, Re_{C1}. The results ($\hat{t}_F$, Re_F) indicated by ● in figure 15 are those obtained for $dRe/d\hat{t} = 0.54\,s^{-1}$ under the influence of an external disturbance at $\hat{f}_I = 5.0$ Hz. From the comparison with the results indicated by ○ in the absence of the external disturbance, it can be seen that, although the primary onset time $\hat{t}_F$ for a constant primary onset Reynolds number Re_F is larger with a disturbance, i.e. for ● than for ○, the

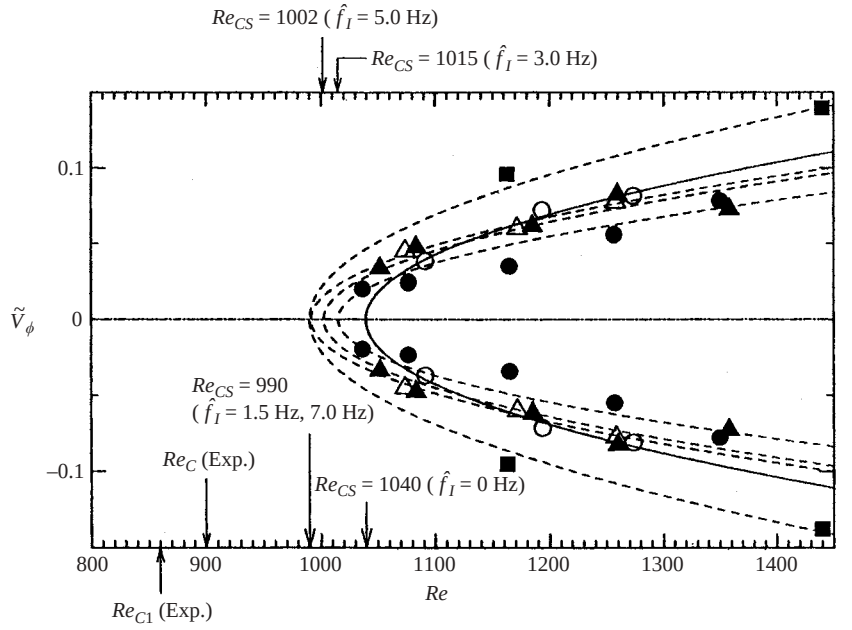

FIGURE 16. Influence of external disturbances with various frequencies $\hat{f}_I$ on the normal-Hopf-bifurcation diagram of the second instability (occurrence of spiral TG vortices) for $\beta = 0.14$. ○, $\hat{f}_I = 0$ Hz (no external disturbance); △, $\hat{f}_I = 1.5$ Hz; ●, $\hat{f}_I = 3.0$ Hz; ▲, $\hat{f}_I = 5.0$ Hz; ■, $\hat{f}_I = 7.0$ Hz. Re_C and Re_{CS} are the critical Reynolds numbers of the first and second instabilities, respectively, and Re_{C1} is the lowest critical Reynolds numbers of the first instability described in § 4.1.

lowest critical Reynolds number Re_{C1} in the former is almost the same as that in the latter. Hence, the external disturbance has no substantial influence on Re_C and Re_{C1}.

4.2. *External-disturbance effect on higher instabilities*

Next, consideration is given to the influence of the external disturbance on the normal and reverse Hopf bifurcations at the onsets of second instability and relaminarization (velocity fluctuation disappearance with increasing R^*), respectively, for $\beta = 0.14$. In the presence of the external disturbance with $\hat{f}_I = 1.5$ Hz, we obtained a bifurcation diagram similar to that in figure 12 without the external disturbance. However, the R_1^* values of the onsets of the second and third instabilities, the disappearance of travelling waves on TG vortices and the onset of the relaminarization shift to lower values, with decreases of 4.8 %, 4.1 %, 7.9 % and 3.6 %, respectively. That is, these higher instabilities are not as robust to the external disturbance as the first instability (Taylor instability), which was uninfluenced by it.

Figure 16 shows the influence of external disturbances with various $\hat{f}_I$ values on the normal-Hopf-bifurcation diagram in the $(Re - \tilde{V}_\phi)$-plane of the second instability (occurrence of spiral TG vortices). Each broken line is a quadratic curve fitted to the experimental data for each $\hat{f}_I$ (the solid line is for $\hat{f}_I = 0$ Hz). Each value of the onset Reynolds number Re_{CS} of the second instability for each $\hat{f}_I$ was determined from the minimum of the quadratic curve. Re_C is the critical Reynolds number of the first instability, and Re_{C1} is the lowest one, as described previously. From figure 16, it is clear that the bifurcation diagram (quadratic curve) and Re_C change considerably

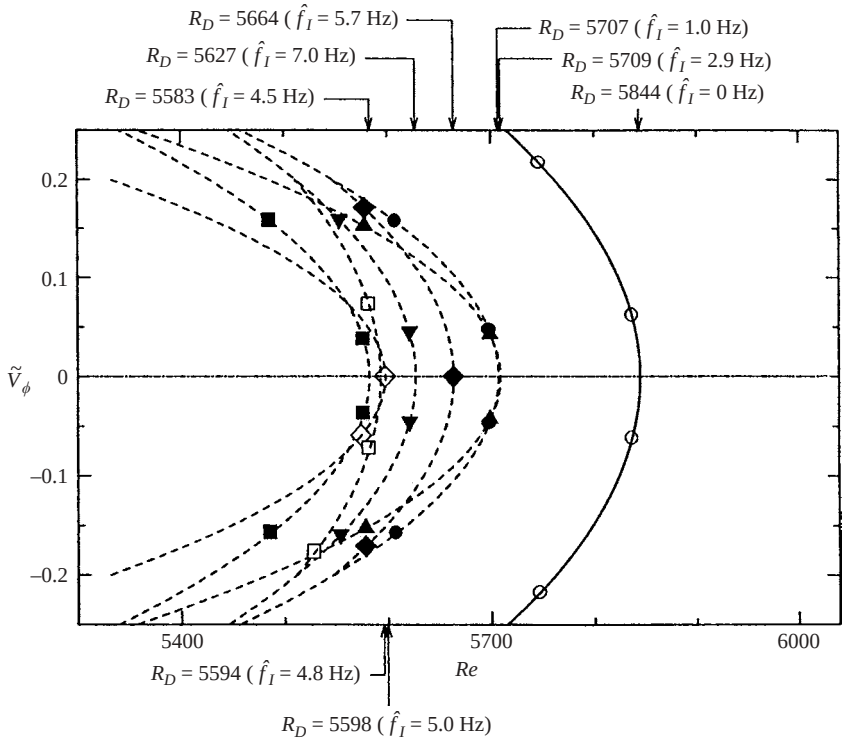

FIGURE 17. Influence of external disturbances with various frequencies $\hat{f}_I$ on the reverse-Hopf-bifurcation diagram of the relaminarization for $\beta = 0.14$. ○, $\hat{f}_I = 0$ Hz (no external disturbance); ●, $\hat{f}_I = 1.0$ Hz; ▲, $\hat{f}_I = 2.9$ Hz; ■, $\hat{f}_I = 4.5$ Hz; □, $\hat{f}_I = 4.8$ Hz; ◇, $\hat{f}_I = 5.0$ Hz; ◆, $\hat{f}_I = 5.7$ Hz; ▼, $\hat{f}_I = 7.0$ Hz. R_D is the onset Reynolds number of the disappearance of velocity fluctuation with increasing Re.

with $\hat{f}_I$. More specifically, Re_{CS} with the external disturbance is smaller than that without it, and is smallest (4.8 %) at $\hat{f}_I = 1.5$ (Δ) and 7.0 (■) Hz.

Figure 17 shows the influence of the external disturbance on the reverse-Hopf-bifurcation diagram (relaminarization) accompanied by no intermittency (Type II intermittency, Berge *et al.* 1984). The bifurcation diagram and the onset Reynolds number R_D of the relaminarization change with $\hat{f}_I$, as in figure 16. R_D with the external disturbance is smaller than that without it, and is smallest (5.4 %) at $\hat{f}_I = 4.5$ Hz (■). From a comparison of the results in figures 16 and 17, it can be seen that the maximum decrease in R_D (5.4 %) from introducing the external disturbance is larger than that in Re_{CS} (4.8 %). Hence, the reverse Hopf bifurcation is more sensitive than the normal Hopf bifurcation to the external disturbance.

4.3. *External-disturbance effect on r.m.s. values and fundamental frequencies of velocity fluctuation*

The influence of the external disturbance on the root-mean-square (r.m.s.) values of velocity fluctuation is considered in the range of about $1.2 \leqslant R_1^* \leqslant 6.6$ between the onsets of the second instability and the relaminarization for $\beta = 0.14$. Figure 18 shows the R_1^* dependence of the r.m.s. value $V_{\theta rms}$ of the fluctuating meridian velocity component $\tilde{V}_\theta$ in the absence and presence of the external disturbance. $V_{\theta rms}$ is not influenced much by the external disturbance with $\hat{f}_I = 1.5$ Hz at about $1.2 \leqslant R_1^* < 2.1$

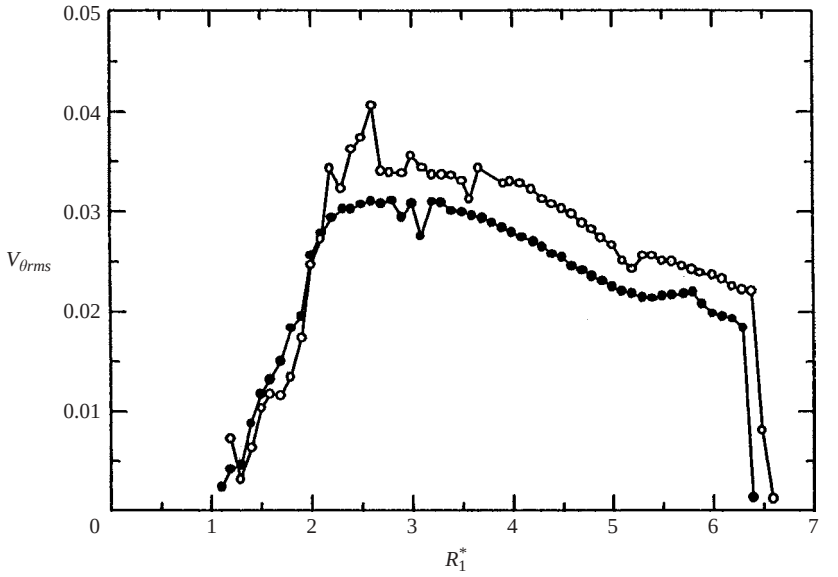

FIGURE 18. Influence of external disturbances with various frequencies $\hat{f}_I$ on the r.m.s. value $V_{\theta rms}$ of $\tilde{V}_\theta$ in the range of about $5 \leqslant R_1^* \leqslant 6.6$ for $\beta = 0.14$. ○, $\hat{f}_I = 0$ Hz (no external disturbance); ●, $\hat{f}_I = 1.0$ Hz; △, $\hat{f}_I = 1.5$ Hz; ▲, $\hat{f}_I = 2.9$ Hz; □, $\hat{f}_I = 4.5$ Hz.

at which the velocity fluctuation increases with R_1^*, but is decreased by the external disturbance both at $2.1 \leqslant R_1^* < 6.3$ at which the velocity fluctuation gradually decreases with increasing R_1^* and at $6.3 \leqslant R_1^* \leqslant 6.6$ at which it abruptly decreases with increasing R_1^*. More specifically, the difference in the external-disturbance effect due to the value of $\hat{f}_I$ appears dominantly just before the velocity fluctuation disappearance, i.e. just before the disappearance of spiral TG vortices.

The following result regarding the onset Reynolds number R_D of the disappearance of fluctuations under the influence of the external disturbance should be noted. The value of R_D determined from the fluctuating meridian velocity component $\tilde{V}_\theta$ (figure 18) is not equal to that obtained from the fluctuating azimuthal velocity component $\tilde{V}_\phi$ (figure 17). The former is slightly larger than the latter. The reason for this is thought to be as follows. Figure 19 shows time series records of fluctuating azimuthal and meridian velocity components, $\tilde{V}_\phi$ and $\tilde{V}_\theta$, respectively, for time $t_1 + 150 \leqslant t \leqslant t_1 + 170$ in the case where R_1^* was first set to be 6.59 at $t = 0$ and then the external disturbance was introduced into the flow at time $t = t_1$. Here, $t_1 = 488$ ($\hat{t}_1 = 10$ minutes). $\tilde{V}_\phi$ changes its waveform instantaneously at $t \approx t_1 + 163$, while $\tilde{V}_\theta$ has not yet changed. As described previously, the external disturbance is given to the meridian velocity component, but the influence of the external disturbance on $\tilde{V}_\theta$ occurs surprisingly slower than on $\tilde{V}_\phi$ as described above. Although the value of R_D was determined at the quasi-static acceleration condition in figure 18, the delay time until the external disturbance influences $\tilde{V}_\theta$ is thought to be larger than that until it influences $\tilde{V}_\phi$. Therefore, the R_D value determined from $\tilde{V}_\theta$ is larger than that determined from $\tilde{V}_\phi$, as described above.

We also considered the influence of external disturbances with various frequencies on the fundamental frequencies of velocity fluctuations caused by spiral TG vortices and travelling waves on TG vortices. It was found that the fundamental frequencies are not influenced by the external disturbance.

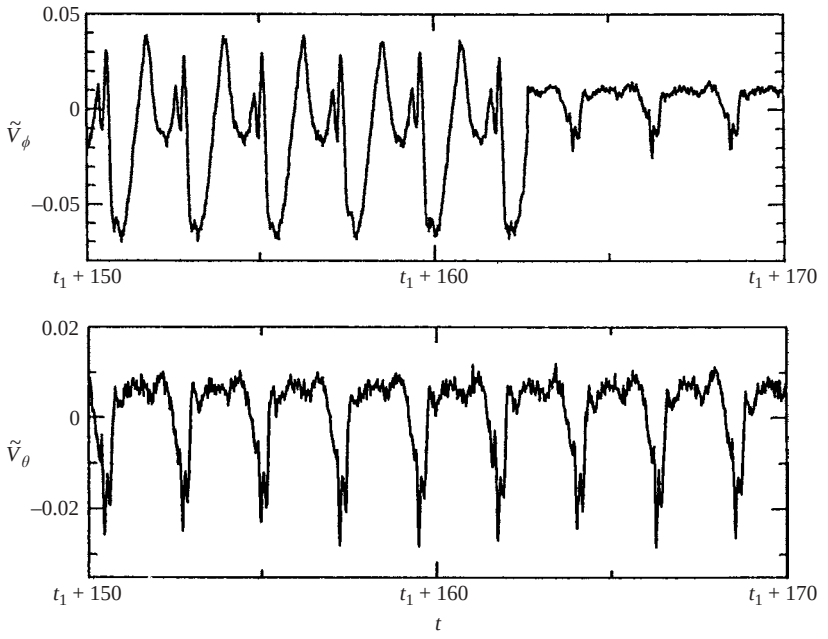

FIGURE 19. Time series records of the fluctuating azimuthal and meridian velocity components for time $t_1 + 150 \leqslant t \leqslant t_1 + 170$ for $\beta = 0.14$ in the case where R_1^* was first set to be 6.59 at $t = 0$ and then the external disturbance with $\hat{f}_I = 1.0$ Hz was introduced into the flow at $t = t_1$. Here, $t_1 = 488$ ($\hat{t}_1 = 10$ minutes).

5. Concluding remarks

In this paper, we have grappled with two important issues regarding spherical Couette flow with the inner sphere rotating and the outer sphere fixed, i.e. the disappearance of velocity fluctuation with increasing Reynolds number Re in the laminar–turbulent transition process (referred to as relaminarization) and the receptivity to a sufficiently small artificial external disturbance introduced into spherical Couette flow.

In order to study relaminarization, we measured velocity fluctuation and investigated the evolution with increasing Re of the velocity power spectra, the kinetic energy, the correlation dimension, the maximum Lyapunov exponent and the probability density distribution of the fluctuating azimuthal velocity component for five clearance ratios: $\beta = 0.06, 0.10, 0.14, 0.158$ and 0.206. For $0.13 < \beta < 0.17$ we found that the relaminarization phenomenon is caused by a reverse Hopf bifurcation with no intermittency, corresponding to the phenomenon that travelling waves on TG vortices degenerate with increasing Reynolds number and finally the flow returns to a completely steady toroidal-TG-vortex flow. In the case with relaminarization, the correlation dimension first increases to 4–5 and then decreases to zero with increasing Re before the occurrence of the relaminarization; it then increases again with Re. In the case without relaminarization, on the other hand, the correlation dimension continues to increase with Re without a decrease. Also, the kinetic energy in the high-frequency components of the fluctuating azimuthal velocity component first increases and later decreases to almost zero with increasing Re in the case with relaminarization, while it continues to increase with Re in the case without relaminarization. Hence, we have obtained new experimental results concerning the phenomenon of velocity fluctuation disappearance

in the present study. However, the dynamics of the relaminarization phenomenon remain unclear, and more theoretical and/or numerical studies are necessary.

Next, in order to study receptivity of the transition process to a sufficiently small artificial external disturbance introduced into the spherical Couette flow, we experimentally examined, with the introduction of an external disturbance, the critical Reynolds numbers of the first and higher instabilities, and the root-mean-square (r.m.s.) values and fundamental frequencies of fluctuating azimuthal and meridian velocity components for $\beta = 0.14$ with relaminarization. We revealed that the lowest critical Reynolds number Re_{C1} of the first instability (Taylor instability) obtained under the condition that the first instability is allowed to take a long time to occur is not influenced by sufficiently small external disturbance. On the other hand, the critical Reynolds numbers of the second instability (occurrence of spiral TG vortices) and the velocity fluctuation disappearance are decreased by the external disturbance. Also, the turbulence intensity can be decreased by the external disturbance at Re values before the velocity fluctuation disappearance. However, fundamental frequencies of spiral TG vortices and travelling waves on TG vortices are not be varied by the external disturbance. Hence, we have experimentally revealed the effects of a small external disturbance on the transition process. The clarification of the mechanism causing these effects requires more theoretical and numerical studies.

This work was supported by a Grant-in-Aid for Scientific Research (C2) in 1996–1997 and 1998–1999 from the Japan Ministry of Education, Science, Sports and Culture.

REFERENCES

Araki, K., Mizushima, J. & Yanase, S. 1997 The nonaxisymmetric instability of the wide-gap spherical Couette flow. *Phys. Fluids* **9**, 1197–1199.

Argyris, J., Faust, G. & Haase, M. 1994 *Texts on Computational Mechanics, Vol. VII, An Exploration of Chaos*, p. 559. North-Holland.

Belyaev, Yu. N., Monakhov, A. A., Scherbakov, S. A. & Yavorskaya, I. M. 1984 Some routes to turbulence in spherical Couette flow. In *Laminar-Turbulent Transition* (ed. V. V. Kozlov), p. 669. Springer.

Belyaev, Yu. N. & Yavorskaya, I. M. 1991 Spherical Couette flow: transitions and onset of chaos. *Fluid Dyn.* **26**, 7–15.

Berge, P., Pomeau, Y. & Vidal, Ch. 1984 *L'Ordre dans le Chaos*, pp. 38, 109, 149. Hermann.

Brandstater, A. & Swinney, H. L. 1987 Strange attractors in weakly turbulent Couette-Taylor flow. *Phys. Rev.* A **35**, 2207–2220.

Bühler, K. 1990 Symmetric and asymmetric Taylor vortex flow in spherical gaps. *Acta Mechanica* **81**, 3–38.

Bühler, K. & Zierep, J. 1984 New secondary flow instabilities for high Re-number flow between two rotating spheres. In *Laminar-Turbulent Transition* (ed. V. V. Kozlov), p. 677. Springer.

Bühler, K. & Zierep, J. 1987 Dynamical instabilities and transition to turbulence in spherical gap flows. *Proc. 1st European Turbulence Conference* (ed. G. Comte-Bellot & J. Mathieu), p. 16. Springer.

Dumas, G. & Leonard, A. 1994 A divergence free spectral expansions method for three-dimensional flows in spherical-gap geometries. *J. Comput. Phys.* **111**, 205–219.

Egbers, C. & Rath, H. J. 1995 The existence of Taylor vortices and wide-gap instabilities in spherical Couette flow. *Acta Mechanica* **111**, 125–140.

Fraser, A. M. & Swinney, H. L. 1986 Independent coordinates for strange attractors from mutual information. *Phys. Rev.* A **33**, 1134–1140.

Krause, E. 1980 Taylor-Görtler vortices in spherical gaps. *Comput. Fluid Dyn.* **2**, 81.

Larger, L., Lee, M. W., Goedgebuer, J. P. & Elflein, W. 2001 Chaos in coherence modulation: bifurcation of an oscillator generating optical delay fluctuations. *J. Opt. Soc. Am.* B-*Opt. Phys.* **18**, 1063–1068.

Longtin, A. & Hinzer, K. 1996 Encoding with bursting, subthreshold oscillations, and noise in mammalian cold receptors. *Neural Computation* **8**, 215–255.

Mamun, C. K. & Tuckerman, L. S. 1995 Asymmetry and Hopf bifurcation in spherical Couette flow. *Phys. Fluids* **7**, 80–91.

Marcus, P. & Tuckerman, L. S. 1987*a* Simulation of flow between concentric rotating spheres. Part 1. Steady states. *J. Fluid Mech.* **185**, 1–30.

Marcus, P. S. & Tuckerman, L. S. 1987*b* Simulation of flow between concentric rotating spheres. Part 2. Transitions. *J. Fluid Mech.* **185**, 31–65.

Munson, B. R. & Menguturk, M. 1975 Viscous incompressible flow between concentric rotating spheres, Part 3. Linear stability and experiments. *J. Fluid Mech.* **69**, 705–719.

Nakabayashi, K. 1978 Frictional moment of flow between two concentric spheres, one of which rotates. *Trans. ASME* I: *J. Fluids Engng* **100**, 97–106.

Nakabayashi, K. 1983 Transition of Taylor-Görtler vortex flow in spherical Couette flow. *J. Fluid Mech.* **132**, 209–230.

Nakabayashi, K., Morinishi, Y. & Kobayashi, M. 1997 Chaotic behavior of the laminar-turbulent transition in spherical Couette flow of clearance ratio $\beta = 0.14$. *Trans. Japan Soc. Mech. Engrs* **63**, 3499–3504 (in Japanese).

Nakabayashi, K. & Sha, W. 2000 Vortical structures and velocity fluctuations of spiral and wavy vortices in the spherical Couette flow. In *Physics of Rotating Fluids* (ed. C. Egbers & G. Pfister). Lecture Notes in Physics, p. 234. Springer.

Nakabayashi, K. & Tsuchida, Y. 1988*a* Spectral study of the laminar-turbulent transition in spherical Couette flow. *J. Fluid Mech.* **194**, 101–132.

Nakabayashi, K. & Tsuchida, Y. 1988*b* Modulated and unmodulated travelling azimuthal waves on toroidal vortices in a spherical Couette system. *J. Fluid Mech.* **195**, 495–522.

Nakabayashi, K. & Tsuchida, Y. 1995 Flow history effect on higher modes in the spherical Couette system. *J. Fluid Mech.* **295**, 43–60.

Nakabayashi, K., Tsuchida, Y. & Zheng, Z. 2002*a* Characteristics of disturbances in the laminar-turbulent transition of spherical Couette flow. Part 1, Spiral Taylor-Görtler vortices and travelling waves for narrow gaps. *Phys. Fluids* **14**, 3963–3972.

Nakabayashi, K., Zheng, Z. & Tsuchida, Y. 2002*b* Evolution of mean and fluctuating velocity components in the laminar-turbulent transition of spherical Couette flow. *Phys. Fluids* **14**, 2839–2846.

Nakabayashi, K., Zheng, Z. & Tsuchida, Y. 2002*c* Characteristics of disturbances in the laminar-turbulent transition of spherical Couette flow. Part 2. New disturbances observed for a medium gap. *Phys. Fluids* **14**, 3973–3982.

Nakabayashi, K., Zheng, Z., Tsuchida, Y. & Morinishi, Y. 1994 Laminar-turbulent transition in spherical Couette flow. In *Laminar-Turbulent Transition* (ed. R. Kobayashi), p. 77. Springer.

Sha, W. & Nakabayashi, K. 2001 On the structure and formation of spiral Taylor-Görtler vortices in spherical Couette flow. *J. Fluid Mech.* **431**, 323–345.

Wimmer, M. 1976 Experiments on a viscous fluid flow between concentric rotating spheres. *J. Fluid Mech.* **78**, 317–335.

Wimmer, M. 1988 Viscous flows and instabilities near rotating bodies. *Prog. Aerospace Sci.* **25**, 43.

Wolf, A., Swift, J. B., Swinney, H. L. & Vastano, J. A. 1985 Determining Lyapunov exponents from a time series. *Physica* **16D**, 285–317.

Wulf, P., Egbers, C. & Rath, H. J. 1999 Routes to Chaos in wide-gap spherical Couette flow. *Phys. Fluids* **11**, 1359–1372.

Yavorskaya, I. M., Belyaev, Yu. N., Monakhov, A. A., Astaf'eva, N. M., Scherbakov, S. A. & Vvedenskaya, N. D. 1980 Stability, nonuniqueness and transition to turbulence in the flow between two rotating spheres. *Rep.* 595. Space Research Institute of the Academy of Science, USSR.

Zikanov, O. Yu. 1996 Symmetry-breaking bifurcations in spherical Couette flow. *J. Fluid Mech.* **310**, 293–324.